INORGANIC CHEMISTRY FRONTIERS

RESEARCH ARTICLE

View Article Online
View Journal

Cite this: DOI: 10.1039/d6qi00392c

Role of M-site cation in the negative linear compressibility of rutile-like $M^{II}(dca)_2$

Muzi Chen, *†[a,b] Hanna L. B. Boström, [c,d] Dominik Daisenberger [e] and Andrew B. Cairns *[a,b]

Received 26th February 2026,
Accepted 15th April 2026

DOI: 10.1039/d6qi00392c

rsc.li/frontiers-inorganic

We investigate the pressure-induced structural deformations in a series of rutile-like network materials, $M(dca)_2$ (M = Mn, Fe, Ni), using synchrotron high-pressure powder X-ray diffraction (HP-PXRD). These materials adopt an orthorhombic structure (space group *Pnnm*) at ambient conditions. All compounds exhibit negative linear compressibility (NLC) along the *c*-axis in their orthorhombic phase ($M(dca)_2$-I), with magnitudes varying across the series: $Mn(dca)_2$ displays the largest NLC of −10(3) TPa^{-1} (0.04–0.3 GPa), while $Ni(dca)_2$ and $Fe(dca)_2$ show −2.5(8) TPa^{-1} (0.07–1.06 GPa) and −2.8(4) TPa^{-1} (0.03–0.95 GPa), respectively. At higher pressures, these compounds undergo second-order phase transitions to a monoclinic structure ($P2_1/n$), with transition pressures dependent on the metal cation.

1 Introduction

Rutile is the most abundant form of TiO_2 and is economically important for its use in refractory ceramics and pigments.[1,2] It has attracted considerable attention in high-pressure research due to the structural origin of a unique mechanical phenomenon known as negative linear compressibility (NLC).[3–5] Certain binary inorganic solids with a rutile structure, such as MgF_2 and TeO_2, expand in at least one linear direction when subjected to hydrostatic compression.[6] This remarkable property arises from the ferroelastic instability inherent in the tetragonal crystal structure of rutile, which comprises edge-sharing octahedral columns connected at their corners.[7,8] Under compression, correlated rotation of adjacent octahedral columns leads to a symmetry lowering from tetragonal to orthorhombic, yielding a $CaCl_2$-type structure.[9–11] To maintain volume continuity across the phase transition, the lattice expands in one of the two directions perpendicular to the column axis.[12]

NLC has great potential for applications in micro- and nanoscale technologies, including pressure sensors, artificial muscles, and actuators.[13,14] While several NLC materials have been identified, ongoing research continues to discover novel materials with enhanced properties.[15–19] Such advances are expected to deepen our understanding of the underlying mechanisms and inform design strategies for NLC materials, ultimately facilitating the transition from fundamental research to practical applications.

Beyond ferroelastic phase transitions in inorganic rutile structures, NLC can also arise through alternative mechanisms. Many coordination polymers, including MOFs and metal cyanides, exhibit NLC attributed to framework hinging.[20–24] In these materials, metal nodes are bridged by flexible molecular ligands to form 1D helical, 2D layered, or 3D wine-rack topologies.[25–27] These structural motifs enable rapid compression along specific directions, which translates into perpendicular expansion *via* framework flexing, producing significant NLC responses. Notable examples include layered Ag(tcm)[25] and the wine-rack structured Cu(tcm),[28] both displaying pronounced anisotropic mechanical behaviours perpendicular to their weakest bonding directions.

The distinct NLC mechanisms observed in rutile-structured inorganics and flexible molecular frameworks inspire the design of a new class of hybrid materials: rutile-structured molecular frameworks. By maintaining the same network topology as their mineral counterparts, these frameworks can exhibit similar mechanical behaviour. Moreover, substituting atomic linkers with molecular ligands introduces additional void space and flexibility, potentially enhancing NLC properties.

The molecular analogues of rutile studied here are transition metal dicyanamides, $M(dca)_2$ (M = Mn, Fe, Co, Ni, Cu). In these compounds, metal ions adopt octahedral MN_6 coordi-

[a]*Department of Materials, Imperial College London, Royal School of Mines, Exhibition Road, SW7 2AZ London, UK. E-mail: a.cairns@imperial.ac.uk; Tel: +44(0)20 7594 9528*
[b]*London Centre for Nanotechnology, Imperial College London, London SW7 2AZ, UK*
[c]*Department of Chemistry, Stockholm University, Svante Arrhenius väg 16C, SE-114 18 Stockholm, Sweden*
[d]*Wallenberg Initiative Materials Science for Sustainability, Department of Chemistry, Stockholm University, SE-114 18 Stockholm, Sweden*
[e]*Diamond Light Source Ltd, Harwell Campus, Didcot OX11 0DE, UK*
†Present address: Department of Heterogeneous Catalysis, Max-Planck-Institut für Kohlenforschung, Kaiser-Wilhelm-Platz 1, D-45470 Mülheim an der Ruhr, Germany. E-mail: muzichen@kofo.mpg.de; Tel: +49(0)176 2873 6256

nation environments similar to rutile.[29] However, unlike the corner-sharing octahedra in rutile, the MN_6 units in $M(dca)_2$ are bridged by three-coordinate dca^- ligands. These linkages occur through the apical amide nitrogen (N2) and terminal nitrile nitrogen (N1) of the dca^- ligands, forming an extended 3D network with a distorted wine-rack topology (Fig. 1).

At ambient conditions, $M(dca)_2$ compounds adopt $CaCl_2$-type orthorhombic structures rather than rutile-type tetragonal structures.[29] Although they do not undergo ferroelastic rutile-to-$CaCl_2$ phase transitions, they exhibit intrinsic NLC under pressure. Previous studies on $Co(dca)_2$ revealed an NLC value of $-3.7(3)$ TPa^{-1} over 0–1.11 GPa,[30] significantly exceeding those of binary inorganic rutile analogues such as MgF_2 ($-1.3(3)$ TPa^{-1}) and MnO_2 ($-0.16(7)$ TPa^{-1}).[6,12] More recently, $Cu(dca)_2$ was found to exhibit an even larger NLC of $-6.5(10)$ TPa^{-1} along the *c*-axis over 0.05–1.11 GPa, attributed to the Jahn–Teller distortion of the Cu^{2+} coordination environment.[31] This pronounced metal-dependent behaviour motivates a systematic investigation across the entire $M(dca)_2$ series to elucidate the role of metal cation identity in determining NLC properties.

In this study, we extend our investigation to the entire $M(dca)_2$ family, including $Mn(dca)_2$, $Fe(dca)_2$, and $Ni(dca)_2$. Using high-pressure powder X-ray diffraction (HP-PXRD), we characterize their structural responses to compression. All compounds exhibit NLC along the *c*-axis, with magnitudes varying significantly with metal cation identity. $Mn(dca)_2$ displays the largest NLC of $-10(3)$ TPa^{-1} over a narrow pressure range (0.04–0.3 GPa), while $Ni(dca)_2$ and $Fe(dca)_2$ show smaller values of $-2.5(8)$ TPa^{-1} (0.07–1.06 GPa) and $-2.8(4)$ TPa^{-1} (0.03–0.95 GPa), respectively. These results reveal the complex interplay between metal cation choice, phase transition behaviour, and NLC properties in this materials family.

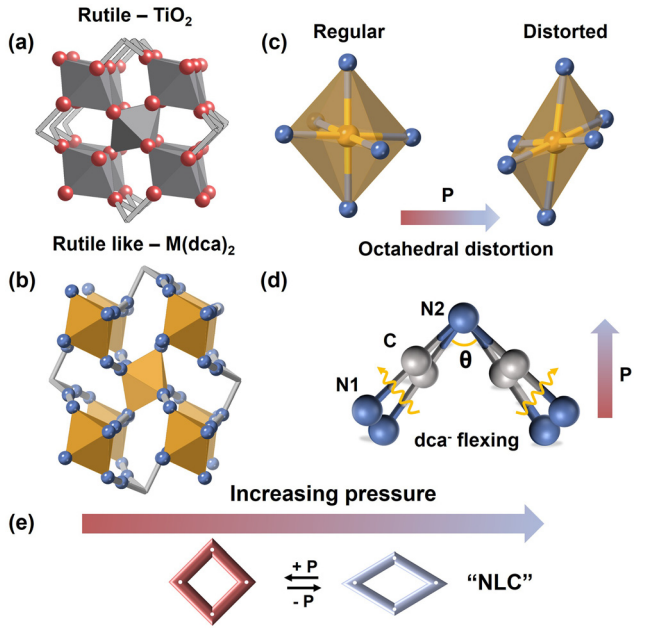

Fig. 1 Structural comparison of rutile-like frameworks and their NLC deformation mechanisms. (a) Rutile TiO_2 and (b) $M(dca)_2$ (M = Mn, Fe, Co, Ni, Cu) both display the characteristic wine-rack topology. The two main pressure-induced deformation mechanisms in $M(dca)_2$ are: (c) octahedral distortion and (d) flexing of "soft" dca^- ligands, where θ represents the C–N2–C bond angle and curved arrows show the ligand movement trajectory. (e) Schematic of the wine-rack compression mechanism exhibiting NLC upon compression.

2 Experimental

2.1 Synthesis

$Mn(dca)_2$: Anhydrous $Mn(dca)_2$ was synthesised following a literature procedure.[32] A hot aqueous solution of Na(dca) (534.3 mg, 6 mmol in 2 mL water) was added to a hot aqueous solution of $Mn(NO_3)_2{\cdot}4H_2O$ (753.03 mg, 3 mmol in 1 mL water). The mixture was heated to boiling for 5 minutes, then transferred to a Petri dish and allowed to evaporate slowly over several days, yielding colourless microcrystals. The product was collected, washed with ethanol (*Note*: water cannot be used due to the high solubility of hydrated $Mn(dca)_2$), and dried at 60 °C overnight. The sample was further heated under vacuum at 100 °C for 5 hours to obtain anhydrous $Mn(dca)_2$, which was then ground into a fine powder.

$Fe(dca)_2$: The synthesis of $Fe(dca)_2$ followed a similar procedure to $Mn(dca)_2$, but using methanol as the solvent due to poor crystallinity when water is used. A hot solution of Na(dca) (534.3 mg, 6 mmol in 4 mL methanol) was added to a hot solution of $Fe(ClO_4)_2{\cdot}6H_2O$ (1088.4 mg, 3 mmol in 4 mL methanol). The mixture was heated at 50 °C for 5 hours, yielding a pale yellow powder. The product was collected, washed sequentially with methanol and ethanol, dried at 60 °C overnight, and evacuated under vacuum at 100 °C for 5 hours to ensure complete desolvation.

$Ni(dca)_2$: A hot aqueous solution of Na(dca) (178.1 mg, 2 mmol in 4 mL water) was added to a hot aqueous solution of $Ni(NO_3)_2{\cdot}6H_2O$ (290.8 mg, 1 mmol in 3 mL water).[33] The mixture was stirred overnight while cooling to room temperature, forming a light blue precipitate. The precipitate was collected by filtration, washed with deionised water, and dried at 60 °C overnight.

2.2 High-pressure powder X-ray diffraction

High-pressure powder X-ray diffraction (HP-PXRD) experiments for $Ni(dca)_2$, $Mn(dca)_2$, and $Fe(dca)_2$ were carried out at the I15 beamline, Diamond Light Source, with an incident wavelength of 0.4246 Å (79 × 79 μm). Finely ground samples were loaded into a 500 μm hole of a steel gasket in a diamond anvil cell (DAC), with Daphne 7373 as the pressure transmitting medium (PTM) and three ruby spheres for pressure calibration. Pressure was determined by ruby fluorescence on-line at the beginning of each diffraction sequence using a Horiba iHR320 spectrometer (473 nm laser). The shift of the R1 fluorescence line of the ruby spheres was measured before and after each data collection, from which the experimental pressure could be calculated. At low pressures (<1 GPa), the error of such measurements is small (typically 0.01 GPa) due

to the minimisation of laser power and exposure time; at higher pressures (>1 GPa), the standard error is usually assumed to be 0.1 GPa.[34] The pressure range was 0.07–3.16 GPa for $Ni(dca)_2$, while $Mn(dca)_2$ and $Fe(dca)_2$ were measured up to 2.78 GPa and 2.44 GPa, respectively, due to weak diffraction signals at high pressures. Diffraction images were collected using a Pilatus3 X CdTe 2M detector located approximately 230 mm from the sample and then integrated and corrected using DAWN software.[35,36]

2.3 Structure refinement and solution

The HP-PXRD patterns were analysed by Rietveld refinement using the TOPAS software.[37,38] Initial structural parameters for the orthorhombic phases were derived from previously reported single-crystal X-ray data for $Ni(dca)_2$ and $Mn(dca)_2$ at ambient conditions.[39,40] In the absence of reported single-crystal X-ray data for $Fe(dca)_2$, its structure was determined by refining the powder diffraction pattern using the $Mn(dca)_2$ model. Structural parameters, including lattice constants and atomic coordinates, were refined against the HP-PXRD patterns. During refinement, the N1–C–N2 linkage was found to remain linear, with the N1–C–N2 angle consistently close to 180°, consistent with the N1≡C triple bond character of the dca^- ligand.

For the high-pressure monoclinic phases of $Ni(dca)_2$, $Mn(dca)_2$, and $Fe(dca)_2$, structural determination was performed in a stepwise manner. Given that these compounds are isostructural with $Co(dca)_2$ under ambient conditions and undergo phase transitions at similar pressures, the HP monoclinic structure of $Co(dca)_2$-II [30] was used as a reference model. Pawley refinement[41] was first performed to determine individual lattice parameters for each compound. These lattice parameters were then fixed during subsequent Rietveld refinement, with atomic coordinates carefully refined to obtain satisfactory fits. This approach successfully determined the structures of the HP monoclinic phases for all three compounds.

2.4 Calculation of bulk moduli and linear compressibilities

Bulk moduli were calculated by fitting the variable-pressure unit cell volume data using the EoSFit7-GUI software.[42] All volume data were fitted using a second-order Birch–Murnaghan equation of state (EoS),[43,44] except for the monoclinic phase of $Fe(dca)_2$, which required a third-order fit. The applicability of the second-order fit was determined by inspection of the *f–F* plots, which visualise the normalised pressure *versus* Eulerian strain data for each phase. A horizontal trend was observed within experimental error for all phases (except $Fe(dca)_2$-II) in these plots, indicating that a second-order Birch–Murnaghan fit sufficiently accounted for the pressure–volume data. Linear compressibility coefficients for each phase were calculated using the PASCal software[45] by correlating lattice parameters with applied pressure.

3 Results

3.1 $Ni(dca)_2$

$Ni(dca)_2$, as a structural analogue of rutile (TiO_2), possesses a single rutile-like network. To investigate its pressure-induced structural behaviour, the compound was characterised by HP-PXRD measurements up to 3.16 GPa. At ambient conditions and low pressures (0.07–1.06 GPa), $Ni(dca)_2$ adopts an orthorhombic structure with space group *Pnnm*. Upon increasing pressure above 1.06 GPa, it undergoes a reversible second-order phase transition to a monoclinic structure with space group $P2_1/n$, and reverts to the orthorhombic phase upon pressure release.

The variable-pressure unit cell volume data for both phases were fitted to the second-order Birch–Murnaghan equation of state (EoS) using EoSFit7-GUI (Fig. 4).[42,46] The bulk modulus decreases from 17.9(4) GPa for the orthorhombic phase (0.07–1.06 GPa) to 15.4(4) GPa for the monoclinic phase (1.21–3.16 GPa), indicating pressure-induced structural softening. This behaviour is counterintuitive, as uniform compression typically leads to bond compaction and increased stiffness. The observed softening can be attributed to the lower symmetry of the monoclinic phase, which permits greater framework flexibility through octahedral distortion and rotation–deformation modes that are symmetry-forbidden in the orthorhombic phase. Under compression, the framework can accommodate stress through relatively low-energy hinging motions rather than direct bond compression, resulting in the observed decrease in bulk modulus.

The linear compressibilities of $Ni(dca)_2$ along the principal crystallographic axes were calculated using PASCal.[45] Over the pressure range of 0.07–1.06 GPa, the orthorhombic phase ($Ni(dca)_2$-I) exhibits negative linear compressibility (NLC) of −2.5(8) TPa^{-1} along the *c*-axis, accompanied by positive linear compressibility (PLC) of 35.7(12) TPa^{-1} and 13.1(5) TPa^{-1} along the *a*- and *b*-axes, respectively.

The NLC behaviour of $Ni(dca)_2$-I arises from a wine-rack breathing mechanism, enabled by the contrasting mechanical properties of its structural components. The Ni^{2+} centres act as rigid nodes, while the dca^- ligands and their coordination bonds serve as flexible hinges. As shown in Fig. 2, the structure contains substantial void space in the *a–b* plane. Under hydrostatic compression, $Ni(dca)_2$-I undergoes rapid contraction along this plane, which is converted into expansion along the perpendicular *c*-axis through flattening of the dca^- ligands.

The dca^- ligand adopts a bent geometry, comprising two N1≡C–N2 moieties. The constituent bonds, characterised by their rigidity, exhibit minimal length changes under compression. Instead, the primary deformation occurs through changes in the dca^- ligand bond angle θ (C–N2–C). As pressure increases from 0.07 to 0.96 GPa, θ increases from 122.6° to 131.6°, while the C≡N bond lengths remain essentially constant (Fig. 2b and Fig. S1). This angular opening directly translates into expansion of the *c* lattice parameter, giving rise to the NLC behaviour. Concurrent with ligand flattening, the NiN_6 octahedra undergo slight distortion: the axial Ni–N2

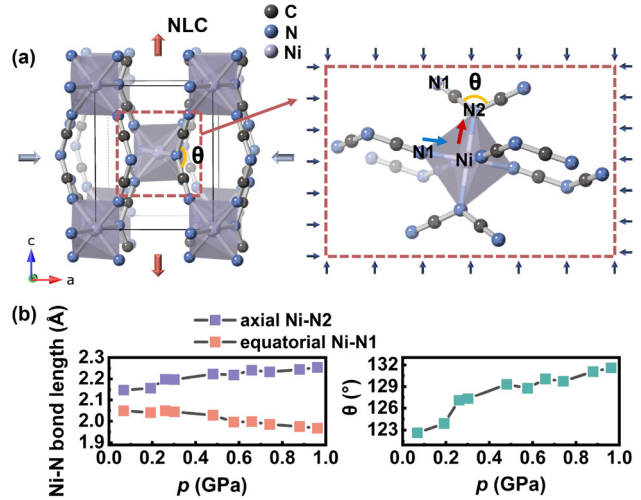

Fig. 2 (a) Illustration of pressure-induced structural deformations in Ni(dca)$_2$-I over a pressure range of 0.07–1.06 GPa. The main deformation mechanisms are the flattening of the dca$^-$ ligands coupled with the octahedral distortion of NiN_6. The blue arrow indicates the contraction of the equatorial Ni–N1 bond, while the red arrow indicates the elongation of the axial Ni–N2 bond. (b) Changes in the dca$^-$ ligand bond angle θ (C–N2–C) and in the Ni–N1 and Ni–N2 bond lengths with increasing pressure.

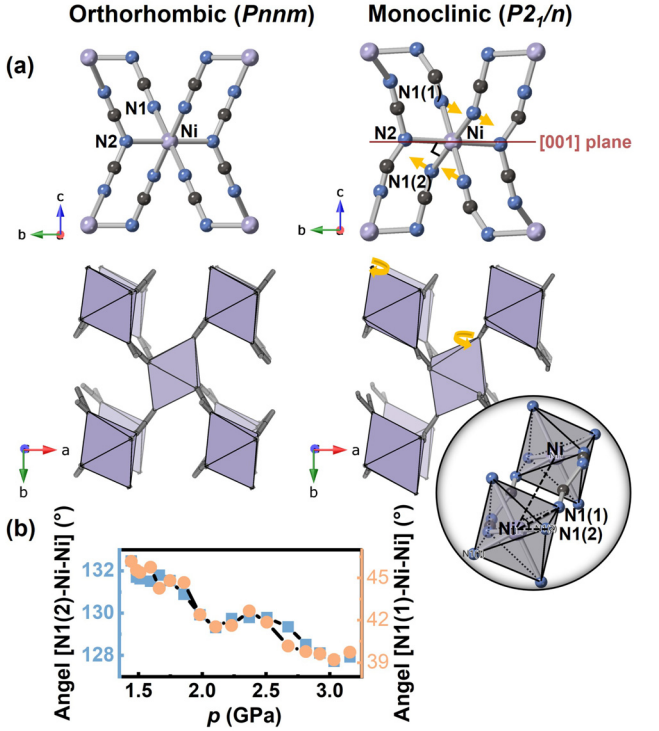

Fig. 3 (a) Crystal structures of Ni(dca)$_2$-I at 0.07 GPa (left) and Ni(dca)$_2$-II at 2.51 GPa (right), viewed along the *a*-axis. Yellow arrows indicate the direction of octahedral rotation in the monoclinic phase. The inset illustrates the octahedral geometry showing the N1(1)–Ni–Ni and N1(2)–Ni–Ni angles used to quantify the rotation. (b) Evolution of these angles with increasing pressure, demonstrating progressive octahedral rotation.

bonds (to the apical nitrogen) elongate, while the equatorial Ni–N1 bonds (to the terminal nitrogen) contract (Fig. 2b).

In the orthorhombic phase Ni(dca)$_2$-I, the dca$^-$ ligands maintain their symmetry, with both N1≡C–N2 moieties remaining coplanar and equivalent in length. However, in the monoclinic phase Ni(dca)$_2$-II, the symmetry is broken, resulting in two crystallographically distinct bonds: N1(1)≡C–N2 and N1(2)≡ C–N2 (Fig. 3). This symmetry reduction leads to further octahedral distortion, with the axial–equatorial bond angles deviating significantly from 90°.

Beyond distortion, the octahedra undergo collective rotation about the [001] direction during compression. This rotation is evidenced by systematic decreases in both the N1(1)–Ni–Ni and N1(2)–Ni–Ni angles with increasing pressure (Fig. 3b), confirming genuine rotational motion rather than simple distortion of the equatorial Ni–N1 bonds. The reduced symmetry of Ni(dca)$_2$-II introduces additional structural degrees of freedom, making the deformation behaviour more complex. Nevertheless, it is clear that framework hinging partially replaces direct bond compression, accounting for the reduced stiffness of Ni(dca)$_2$ at high pressures.

Unlike Ni(dca)$_2$-I, the monoclinic phase Ni(dca)$_2$-II does not exhibit NLC. This loss of NLC behaviour can be attributed to the disruption of the cooperative wine-rack hinging mechanism that characterises the orthorhombic phase. In Ni(dca)$_2$-II, the symmetry breaking introduces multiple independent deformation modes—including octahedral rotation, asymmetric ligand distortion, and varied bond angle changes—that compete with the directional expansion mechanism. The dominance of octahedral rotation, evidenced by systematic changes in the N1–Ni–Ni angles (Fig. 3b), allows the structure to accommodate compression more isotropically. Consequently, Ni(dca)$_2$-II shows PLC along all three principal axes, with values of 18.8(10) TPa^{-1}, 17.8(6) TPa^{-1}, and 9.4(7) TPa^{-1} along *a*, *b*, and *c*, respectively, over the pressure range of 1.21–3.16 GPa.

3.2 Mn(dca)$_2$

Mn(dca)$_2$ adopts a rutile-like structure similar to Ni(dca)$_2$, with Mn^{2+} ions octahedrally coordinated to six dca$^-$ ligands. However, due to the larger ionic radius of Mn^{2+} compared to Ni^{2+},[47] the metal–ligand bonds are longer. Specifically, the axial Mn–N2 bond in Mn(dca)$_2$ measures 2.5 Å, while the equatorial Mn–N1 bond is 2.3 Å, both substantially exceeding the corresponding bonds of 2.1 Å and 2.2 Å in Ni(dca)$_2$. Consequently, the orthorhombic unit cell of Mn(dca)$_2$ is larger, with lattice parameters a = 6.1352(9) Å, b = 7.3046(9) Å, c = 7.5317(12) Å, and volume V = 337.53(9) Å^3 at ambient conditions.

HP-PXRD studies reveal that Mn(dca)$_2$ exhibits distinctly different pressure-induced behaviour compared to Ni(dca)$_2$. While Ni(dca)$_2$ maintains its orthorhombic structure up to 1.1 GPa, the orthorhombic phase of Mn(dca)$_2$ (Mn(dca)$_2$-I) persists only up to 0.3 GPa (Fig. 4). At this pressure, Mn(dca)$_2$ undergoes a second-order phase transition to a monoclinic structure with $P2_1/n$ symmetry. Critically, despite sharing the same

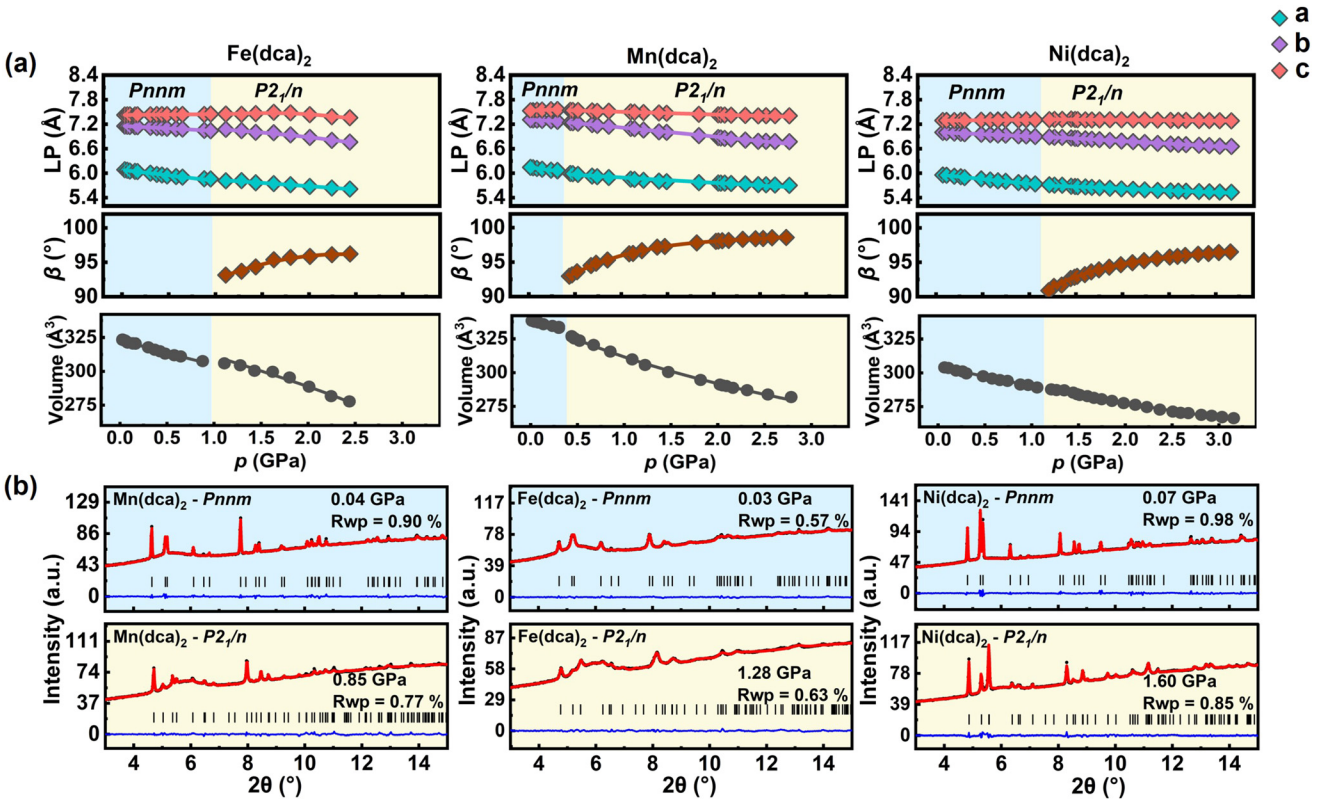

Fig. 4 (a) Changes in lattice parameters and volume as a function of pressure for $Ni(dca)_2$, $Mn(dca)_2$, and $Fe(dca)_2$. Background colours indicate structural phases: orthorhombic (blue) and monoclinic (cream). Lattice parameters were fitted linearly for both phases, with the monoclinic β angle fitted to a third-order polynomial. Volume data were fitted using the second-order Birch–Murnaghan equation of state (third-order for $Fe(dca)_2$-II). (b) Representative HP-PXRD patterns with Rietveld refinements: experimental data (black), calculated fit (red), difference curve (grey), and tick marks indicate allowed reflections.

space group as $Ni(dca)_2$-II, the monoclinic phase $Mn(dca)_2$-II exhibits a fundamentally different topology: the axial Mn–N2 coordination bonds elongate dramatically to ~3.0 Å, effectively becoming van der Waals contacts, resulting in a staggered stacking arrangement of highly distorted octahedra (Fig. 6a). This contrasts sharply with $Ni(dca)_2$-II, which maintains octahedral coordination with only minor displacement of atoms from their orthorhombic positions.

Investigation of the pressure-induced deformation in $Mn(dca)_2$-I reveals that the dominant mechanism differs from that in $Ni(dca)_2$-I. Rather than compression-induced flattening of dca^- ligands, the primary deformation involves distortion of the MnN_6 octahedra through a shear hinging motion of the framework. The spacious unit cell along the *a*–*b* plane permits substantial structural rearrangement under compression. As the pressure increases, coordinated reorientation of both the axial Mn–N2 bonds and the equatorial Mn–N1 bonds occurs, breaking the octahedral symmetry (Fig. 5b). This shear-like deformation causes the octahedral bond angle φ (N2–Mn–N1) to deviate significantly from the ideal 90°, providing a low-energy pathway to accommodate hydrostatic stress without significant bond compression.

The evolution of the octahedral bond angle φ with pressure is shown in Fig. 5c. The systematic decrease of φ indicates progressive octahedral distortion within $Mn(dca)_2$-I, with a dramatic drop at 0.3 GPa accompanied by substantial changes in other structural parameters, including the dca^- ligand bond angle θ (C–N2–C) and the N1≡C–N2 bond lengths (see Fig. S2). These abrupt changes suggest that $Mn(dca)_2$-I approaches the limit of its structural stability at this critical pressure. The large octahedral distortion φ decrease of 16.2° over the narrow pressure range of 0–0.3 GPa can be attributed to the spacious unit cell, which accommodates structural rearrangement under compression. Concurrent with octahedral distortion, the dca^- ligands deform in response to the coordinated reorientation of metal–ligand bonds. As both Mn–N2 and Mn–N1 bonds reorient under compression, the dca^- ligands are pulled in opposite directions along the framework, resulting in changes to the dca^- ligand bond angle θ (C–N2–C) (Fig. 5b and c).

Linear compressibilities calculated using PASCal reveal positive values of 34(8) TPa^{-1} and 20(2) TPa^{-1} along the *a*- and *b*-axes, respectively, but a remarkable NLC of −10(3) TPa^{-1} along the *c*-axis over 0–0.3 GPa. This represents the most pronounced NLC in the entire series, approximately four times larger than that observed in $Ni(dca)_2$-I. This counterintuitive behaviour arises from competing geometric effects. Detailed analysis reveals that the coordination angle γ (C–N1–Mn),

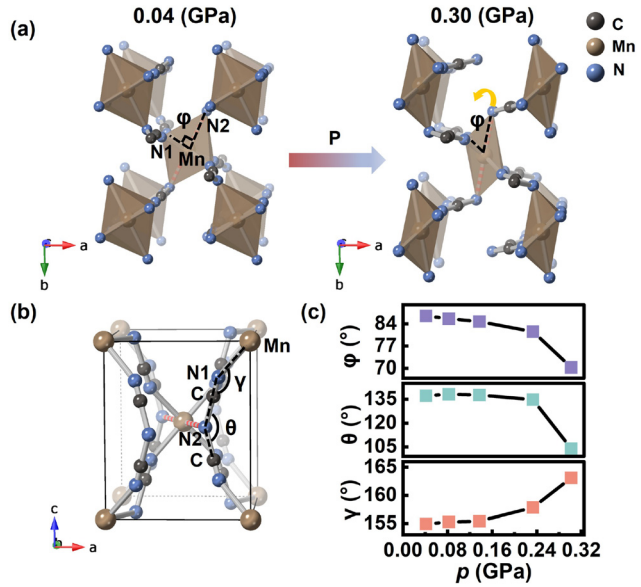

Fig. 5 Pressure-induced structural evolution of $Mn(dca)_2$-I. (a) Octahedral packing viewed along the *c*-axis at 0.04 GPa (left) and 0.30 GPa (right). The yellow arrow indicates ligand rotation under compression. (b) Simplified view at 0.04 GPa with octahedra removed, showing three key angles: φ (octahedral bond angle, N2–Mn–N1), θ (dca^- ligand bond angle, C–N2–C), and γ (coordination angle, C–N1–Mn). (c) Evolution of these angles with pressure.

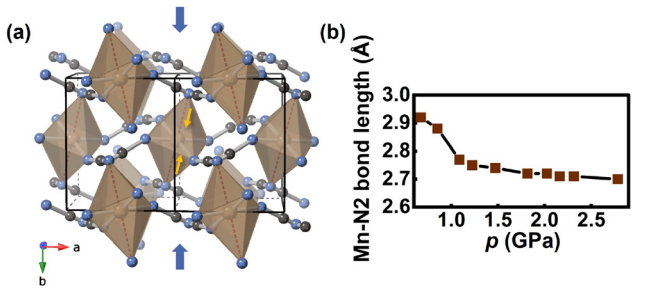

Fig. 6 (a) Crystal structure of $Mn(dca)_2$-II at 1.09 GPa, viewed along the *c*-axis, showing the staggered stacking structure resulting from elongated Mn–N2 bonds. (b) Evolution of the Mn–N2 bond length as a function of pressure.

which governs the connection between the terminal N1 of dca^- and the Mn centres, increases with pressure (Fig. 5c). This angular opening, driven by the reorientation of the Mn–N1 bonds, increases the projection of the coordination bond length along the *c*-axis. The net deformation along the *c*-axis can thus be understood as a competition between the contracting influence of decreasing θ and the expanding influence of increasing γ. In $Mn(dca)_2$-I, the latter effect dominates due to the framework spaciousness, resulting in the observed enhanced NLC behaviour. The bulk modulus of $Mn(dca)_2$-I is 18.2(7) GPa, comparable to that of $Ni(dca)_2$-I (17.9 GPa) despite the larger unit cell.

Above 0.3 GPa, the orthorhombic structure collapses and $Mn(dca)_2$ transforms to the monoclinic phase $Mn(dca)_2$-II. The phase transition is accompanied by a dramatic elongation of the axial Mn–N2 bonds, while the equatorial Mn–N1 distances remain relatively constant (Fig. 6b). The exceptionally long Mn–N2 bond (approaching 3 Å) suggests a transition from traditional coordination bonding to van der Waals-type interactions, reducing the material's stiffness. This is reflected in the bulk modulus of $Mn(dca)_2$-II, which decreases to 9.6(2) GPa substantially lower than the orthorhombic phase value.

The weakened axial bonding produces a staggered stacking structure with considerable void space along the *b*-axis (Fig. 6a), resulting in highly anisotropic compressibility. The Mn–N2 distance decreases rapidly with increasing pressure (Fig. 6b), corresponding to compression of the van der Waals gap. Accordingly, $Mn(dca)_2$-II exhibits the highest compressibility along the *b*-axis (26.6(13) TPa^{-1}) and smaller values along the *a*- and *c*-axes (17.9(15) TPa^{-1} and 10.4(12) TPa^{-1}, respectively) over the pressure range of 0.44–2.78 GPa.

3.3 $Fe(dca)_2$

$Fe(dca)_2$ is isostructural with $Ni(dca)_2$ and $Mn(dca)_2$, with Fe^{2+} occupying the octahedral metal sites. Unlike the other two compounds, $Fe(dca)_2$ has nearly identical axial Fe–N2 and equatorial Fe–N1 bonds, both measuring 2.4 Å. At ambient conditions, $Fe(dca)_2$ adopts an orthorhombic structure with space group *Pnnm* and lattice parameters a = 6.086(3) Å, b = 7.155(3) Å, c = 7.425(3) Å, and V = 323.3(2) $Å^3$. Although Fe^{2+} and Mn^{2+} have close ionic radii, resulting in similar unit cell sizes for $Fe(dca)_2$ and $Mn(dca)_2$, the two compounds exhibit markedly different pressure-induced behaviour.

HP-PXRD studies reveal that $Fe(dca)_2$ undergoes a phase transition from orthorhombic to monoclinic ($P2_1/n$) at approximately 1.0 GPa (Fig. 4). This transition pressure is similar to that of $Ni(dca)_2$ (1.06 GPa) but substantially higher than that of $Mn(dca)_2$ (0.3 GPa), indicating that the orthorhombic phase $Fe(dca)_2$-I exhibits greater structural stability under compression. Interestingly, despite the similar transition pressures, the monoclinic phase $Fe(dca)_2$-II adopts the structural model of $Mn(dca)_2$-II rather than $Ni(dca)_2$-II, featuring a staggered stacking arrangement of highly distorted octahedra.

The compression behaviour of $Fe(dca)_2$-I closely resembles that of $Mn(dca)_2$-I, characterised by pronounced octahedral distortion through a shear hinging mechanism. As shown in Fig. 7a and b, the octahedral bond angle φ (N2–Fe–N1) increases by more than 10° over the pressure range of 0.03–0.95 GPa. This distortion results from coordinated reorientation of both Fe–N2 and Fe–N1 bonds, breaking the octahedral symmetry. The relatively spacious framework along the *a*–*b* plane facilitates this deformation, allowing the structure to accommodate compression through low-energy hinging motions. The octahedral distortion drives expansion along the perpendicular *c*-axis *via* geometric coupling through the dca^- ligands.

Linear compressibilities calculated using PASCal reveal positive values of 40(3) TPa^{-1} and 16.8(7) TPa^{-1} along the

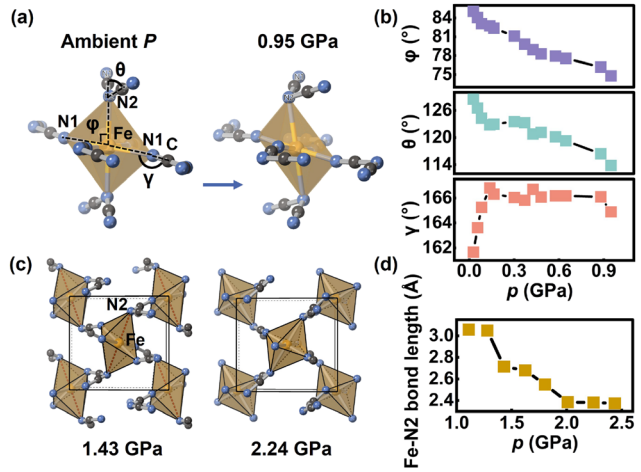

Fig. 7 Pressure-induced structural evolution of $Fe(dca)_2$. (a) Octahedral packing of $Fe(dca)_2$-I at 0.03 GPa and 0.95 GPa, viewed along the *c*-axis, illustrating the deformation mechanism under compression. (b) Evolution of key structural angles with pressure: φ (octahedral bond angle, ∠N2–Fe–N1), θ (dca^- ligand bond angle, ∠C–N2–C), and γ (coordination angle, ∠C–N1–Fe). (c) Crystal structures of $Fe(dca)_2$-II at 1.43 GPa and 2.24 GPa, viewed along the *b*-axis, showing the elongated Fe–N2 bond. (d) Evolution of the Fe–N2 bond length as a function of pressure.

a- and *b*-axes, respectively, and negative linear compressibility (NLC) of −2.8(4) TPa^{-1} along the *c*-axis. The bulk modulus of $Fe(dca)_2$-I is 14.8(4) GPa, slightly lower than those of $Ni(dca)_2$-I (17.9 GPa) and $Mn(dca)_2$-I (18.2 GPa).

The NLC magnitude of $Fe(dca)_2$-I (−2.8(4) TPa^{-1}) is comparable to that of $Ni(dca)_2$-I (−2.5(8) TPa^{-1}) but substantially smaller than $Mn(dca)_2$-I (−10(3) TPa^{-1}). This variation demonstrates that the NLC properties of these isostructural compounds depend sensitively on the identity of the metal cation, the available framework space, and the pressure range over which the orthorhombic phase remains stable.

Above 1.0 GPa, $Fe(dca)_2$ transforms to the monoclinic phase $Fe(dca)_2$-II, which features a staggered stacking structure with an exceptionally long axial Fe–N2 bond, creating substantial void space along the *c*-axis (Fig. 7c). Similar to $Mn(dca)_2$-II, the predominant deformation in $Fe(dca)_2$-II is rapid contraction along the direction of the elongated Fe–N2 interaction (Fig. 7d).

However, $Fe(dca)_2$-II exhibits a behaviour that distinguishes it from $Mn(dca)_2$-II. While the Mn–N2 bond in $Mn(dca)_2$-II contracts to a plateau length of approximately 2.7 Å, the Fe–N2 bond in $Fe(dca)_2$-II continues to decrease, reaching 2.4 Å at 2.0 GPa (Fig. 7d). This value approaches the typical Fe–N coordination bond length, indicating reformation of a covalent Fe–N2 bond. This phenomenon suggests that $Fe(dca)_2$-II undergoes a pressure-induced transition from a van der Waals-bonded staggered structure to a more conventional coordination geometry, representing a transition to a lower-energy configuration at high pressure.

The distinct compression behaviour of $Fe(dca)_2$-II is also reflected in its equation of state. Unlike $Mn(dca)_2$-II, which is well described by a second-order Birch–Murnaghan equation, $Fe(dca)_2$-II requires a third-order fit, yielding a bulk modulus B_0 = 14.67(7) GPa and its pressure derivative B'_0 = 0.2(3). The unusually low value of B'_0 (typically $B'_0 \approx 4$ for most materials) indicates anomalous softening behaviour: the material becomes more compliant with increasing pressure. This counterintuitive trend can be rationalised by the structural transformation occurring within the monoclinic phase, as the weakly bonded staggered structure gradually transitions toward a more conventional coordination framework through Fe–N2 bond reformation.

4 Discussion

The three isostructural $M(dca)_2$-I compounds (M = Mn, Fe, Ni) all exhibit NLC along the *c*-axis, but with different magnitudes (Table 1 and Fig. 8a). $Mn(dca)_2$-I shows the most pronounced NLC of −10(3) TPa^{-1} over the narrow pressure range of 0–0.3 GPa. $Fe(dca)_2$-I exhibits a more moderate NLC of −2.8(4) TPa^{-1} over 0.03–0.95 GPa, while $Ni(dca)_2$-I displays the smallest NLC of −2.5(8) TPa^{-1} over 0.07–1.06 GPa. This systematic variation is discussed in detail below in terms of framework spaciousness and deformation mechanism.

The observed trend correlates directly with metal cation size. Larger cations such as Mn^{2+} create more spacious frameworks with greater void volume along the *a*–*b* plane. This increased space permits substantial framework deformation through hinging mechanisms, resulting in pronounced NLC effects. Conversely, smaller cations such as Ni^{2+} yield more compact

Table 1 Compressibilities and bulk moduli of $M(dca)_2$ (M = Ni, Mn, Fe, and Cd)

Material	K_a (TPa^{-1})	K_b (TPa^{-1})	K_c (TPa^{-1})	B_0 (GPa)	B'	Pressure range (GPa)
$Ni(dca)_2$-I	35.75	13.11	−2.47	17.9(4)	4	0.07–1.06
$Ni(dca)_2$-II	18.81	17.82	9.45	15.9(4)	4	1.21–3.16
$Mn(dca)_2$-I	34.27	20.07	−10.30	18.2(7)	4	0.04–0.30
$Mn(dca)_2$-II	17.90	26.62	10.42	9.6(2)	4	0.44–2.78
$Fe(dca)_2$-I	40.32	16.82	−2.79	14.9(4)	4	0.03–0.95
$Fe(dca)_2$-II	33.66	37.83	17.66	14.6(7)	0.2(3)	1.11–2.44
$Cd(dca)_2$[a]	42(2)	28.0(3)	22.5(7)	7.0(3)	6.1(5)	0.05–2.33

[a] $Cd(dca)_2$ adopts the monoclinic $P2_1/n$ structure throughout the entire measured pressure range and does not form the orthorhombic NLC-active phase. All compressibilities are positive; no NLC is observed.

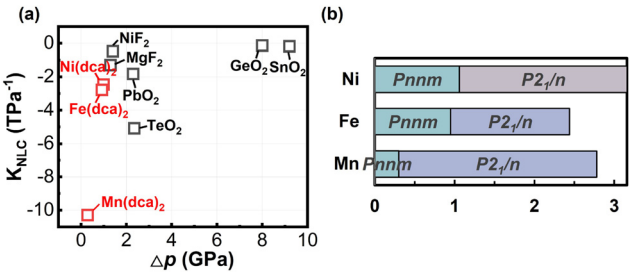

Fig. 8 (a) Correlation between NLC magnitude and pressure range for $M(dca)_2$ (M = Ni, Mn, Fe) and rutile-structured dioxides and difluorides. The molecular framework materials exhibit systematically larger NLC values than their inorganic analogues. (b) Phase diagram for the $M(dca)_2$ series, showing the orthorhombic–monoclinic phase transition pressure for each metal cation.

structures with restricted deformation capacity, leading to smaller NLC magnitudes. This behaviour parallels that observed in rutile-structured binary oxides and fluorides, where larger cations consistently produce more pronounced NLC responses. For example, TeO_2 exhibits the largest NLC of -5.1 TPa^{-1} among rutile dioxides, attributed to its large Te^{4+} cation.[6]

The cation size effect extends beyond NLC magnitude to govern structural stability. Mn^{2+}, with the largest ionic radius among the three compounds (0.83 Å),[47] represents a structural tipping point: its framework undergoes exceptionally rapid octahedral distortion ($\Delta\varphi$ = 16.2° over 0–0.3 GPa), producing the largest NLC of $-10(3)$ TPa^{-1} but collapsing to the monoclinic phase at only 0.3 GPa. Attempts to extend the series to larger cations confirm this boundary. Cd^{2+} (0.95 Å),[47] the next larger candidate, crosses the structural tolerance limit entirely: $Cd(dca)_2$ does not adopt the orthorhombic rutile-like structure at ambient conditions, instead forming a monoclinic phase, and consequently exhibits no NLC (Table 1 and Fig. S11). This directly confirms that the cation-size threshold for the NLC-enabling orthorhombic framework lies between Mn^{2+} (0.83 Å) and Cd^{2+} (0.95 Å). Similarly, $Zn(dca)_2$, with the smaller Zn^{2+} cation and preference for tetrahedral coordination, organises into a buckled layered structure incompatible with the rutile topology.[48,49] These observations establish that the NLC-enabling orthorhombic framework is stable only within a specific cation-size window, and that Mn^{2+} sits at its upper boundary, maximising NLC within this family through cation-size tuning alone.

Beyond cation size, the nature of the bridging ligand plays a crucial role in determining NLC properties. The $M(dca)_2$ series consistently exhibits more pronounced NLC compared to rutile-structured inorganic compounds (Fig. 8a), despite sharing the same underlying topology. This enhancement arises from the substitution of rigid oxide/fluoride linkages with flexible molecular dca^- ligands. The molecular ligands and their coordination to metal centres represent structural "soft modes" that can accommodate compression through low-energy deformations, reducing the need for compression of individual bonds. This flexibility enables efficient conversion of rapid compression along the *a*–*b* plane into expansion along the perpendicular *c*-axis through framework hinging, amplifying the NLC response.

Within the $M(dca)_2$ series, the compression-induced deformation of $M(dca)_2$-I compounds involves two primary mechanisms: modification of the dca^- ligand bond angle θ (C–N2–C) and distortion of the MN_6 octahedra (quantified by the octahedral bond angle φ between axial and equatorial M–N bonds). Both mechanisms contribute to NLC, but their relative importance varies across the series. In $Ni(dca)_2$-I, ligand flattening dominates: the dca^- ligand bond angle θ increases from 122.6° to 131.6° over 0.07–0.96 GPa. Because the dca^- ligands are oriented primarily along the *c*-axis, this angular opening directly drives lattice expansion along this direction.

In contrast, $Mn(dca)_2$-I and $Fe(dca)_2$-I are dominated by octahedral distortion through a shear hinging mechanism. These compounds exhibit dramatic changes in the octahedral bond angle φ (exceeding 10°) as both axial M–N2 and equatorial M–N1 bonds reorient under compression. This coordinated reorientation pulls the dca^- ligands in opposite directions, altering their coordination geometry and increasing the coordination angle γ (C–N1–M). The increased γ enhances the projection of the coordination bonds along the *c*-axis, driving lattice expansion despite simultaneous decreases in the dca^- ligand bond angle θ.

The divergent deformation modes arise directly from differences in framework spaciousness. Ni^{2+}, with shorter M–N bonds and a more compact framework, provides insufficient space for significant octahedral shearing, so the structure accommodates compression primarily through ligand bending, resulting in a smaller NLC of -2.47 TPa^{-1}. In contrast, Fe^{2+}, with longer M–N bonds and a more spacious framework, provides sufficient space for octahedral shear hinging, yielding a larger NLC of -2.79 TPa^{-1}. $Mn(dca)_2$ shares the same shear hinging mechanism as $Fe(dca)_2$, but the dramatically larger NLC of $-10(3)$ TPa^{-1} arises because Mn^{2+} sits at the upper limit of the structural tolerance window, where the framework undergoes exceptionally large-amplitude deformation before collapse (Fig. 8b). As established above, both NLC magnitude and transition pressure are co-consequences of framework spaciousness rather than causally linked.

The specific deformation pathways in the orthorhombic phases determine the nature of the resulting high-pressure monoclinic structures. $Ni(dca)_2$-II undergoes relatively minor structural rearrangement, with octahedra only slightly displaced from their original positions, a consequence of the symmetry-breaking transition occurring in an already compact structure. In contrast, $Mn(dca)_2$-II and $Fe(dca)_2$-II exhibit dramatically different structures featuring staggered stacking of highly distorted octahedra. This structural reorganization involves breaking of the axial M–N2 coordination bonds and their replacement by van der Waals interactions with bond lengths approaching 3.0 Å, creating substantial void space along specific crystallographic directions.

These structural differences lead to distinct high-pressure compression mechanisms. $Ni(dca)_2$-II deforms through contin-

ued octahedral distortion and rotation enabled by reduced symmetry constraints. $Mn(dca)_2$-II and $Fe(dca)_2$-II, by contrast, compress primarily through contraction of the weakly bound staggered layers along the extended M–N2 directions. Notably, $Fe(dca)_2$-II exhibits unique behaviour: its Fe–N2 separation continuously decreases under compression, ultimately reforming covalent Fe–N coordination bonds by 2 GPa and transitioning the structure toward a more conventional coordination geometry. This behaviour, absent in $Mn(dca)_2$-II, reflects subtle differences in electronic structure and bonding preferences between Fe^{2+} and Mn^{2+}.

The insights gained from the $M(dca)_2$ series motivate further exploration of chemical modification as a strategy to optimise NLC in this materials family. Our prior and ongoing work demonstrates that both M-site substitution and ligand substitution represent viable but distinct design levers. Substitution of Cu^{2+} at the M-site, which introduces a Jahn–Teller coordination environment, yields a larger NLC of $-6.5(10)$ TPa^{-1} in $Cu(dca)_2$ while preserving a comparable transition pressure to the Ni and Fe analogues. This demonstrates that electronic modification of the metal centre can enhance NLC magnitude without sacrificing the pressure stability window.[31] Ligand substitution with the stiffer tricyanomethanide anion (tcm^-, $C(CN)_3^-$), which forms topologically related but doubly interpenetrating rutile-like $M(tcm)_2$ frameworks, raises structural stability substantially, with no phase transition observed in $M(tcm)_2$ (M = Ni, Co, Fe, Mn) up to ~3 GPa, but suppresses NLC entirely, with the $M(tcm)_2$ series showing only small positive linear compressibility along the *c*-axis.[31,50] Taken together, these efforts highlight a key design challenge: achieving simultaneously large NLC magnitude and a wide pressure stability window requires balancing framework flexibility with structural robustness, and identifying viable strategies to achieve this remains an open question for future work.

5 Conclusion

This systematic investigation of the $M(dca)_2$ series (M = Ni, Mn, Fe) reveals how metal cation and framework topology govern negative linear compressibility (NLC) in rutile-like molecular frameworks. All compounds exhibit NLC along the *c*-axis arising from their shared wine-rack topology, with magnitudes varying fourfold from $-2.5(8)$ TPa^{-1} in $Ni(dca)_2$ to $-10(3)$ TPa^{-1} in $Mn(dca)_2$. This correlates with cation size: larger cations create more spacious frameworks that accommodate substantial shear-type octahedral distortions, while smaller cations yield compact structures where deformation is restricted to ligand bending.

These structure–property relationships establish the $M(dca)_2$ series as a tunable platform for designing materials with tailored anisotropic compressibility. The consistently enhanced NLC responses compared to inorganic rutile materials, coupled with the chemical stability and processability of dicyanamide-based frameworks, position this family as promising candidates for practical applications in pressure sensors, actuators, and mechanical metamaterials.[13]

Author contributions

M. C.: conceptualization, methodology, investigation, formal analysis, writing – original draft. H. L. B. B.: investigation, writing – review & editing. D. D.: investigation, writing – review & editing. A. B. C.: conceptualisation, investigation, supervision, project administration, funding acquisition, writing – review & editing.

Conflicts of interest

There are no conflicts to declare.

Data availability

The data supporting this article have been included as part of the supplementary information (SI). Supplementary information is available. See DOI: **https://doi.org/10.1039/d6qi00392c**.

Acknowledgements

We thank the Diamond Light Source (proposal number CY29285) for the provision of beamtime. HLBB acknowledges financial support from the Swedish Research Council (VR, grant number 2022-02984) and the Wallenberg Initiative Materials Science for Sustainability (WISE), funded by the Knut and Alice Wallenberg Foundation. Open Access funding provided by the Max Planck Society.

References

1 D. A. Hanaor and C. C. Sorrell, *J. Mater. Sci.*, 2011, **46**, 855–874.
2 N. Gonzalez Szwacki, P. Fabrykiewicz, I. Sosnowska, F. Fauth, E. Suard and R. Przeniosło, *J. Phys. Chem. C*, 2023, **127**, 19240–19249.
3 J. C. Jamieson and B. Olinger, *Science*, 1968, **161**, 893–895.
4 L. Gerward and J. Staun Olsen, *J. Appl. Crystallogr.*, 1997, **30**, 259–264.
5 Z. Tang, J. Zhang, Z. Cheng and Z. Zhang, *Mater. Chem. Phys.*, 2003, **77**, 314–317.
6 L. Ming, M. Manghnani, T. Matsui and J. Jamieson, *Phys. Earth Planet. Inter.*, 1980, **23**, 276–285.
7 A. F. Wells, *Structural Inorganic Chemistry*, Oxford University Press, 2012.
8 S. R. Dhage, R. Pasricha and V. Ravi, *Mater. Res. Bull.*, 2003, **38**, 1623–1628.
9 J. Haines, J. Léger and S. Hoyau, *J. Phys. Chem. Solids*, 1995, **56**, 965–973.

10 J. Haines and J. Léger, *Phys. Rev. B: Condens. Matter Mater. Phys.*, 1997, **55**, 11144.
11 P. Peercy, I. Fritz and G. Samara, *J. Phys. Chem. Solids*, 1975, **36**, 1105–1122.
12 A. B. Cairns and A. L. Goodwin, *Phys. Chem. Chem. Phys.*, 2015, **17**, 20449–20465.
13 R. H. Baughman, S. Stafstrom, C. Cui and S. O. Dantas, *Science*, 1998, **279**, 1522–1524.
14 R. H. Baughman, *Nature*, 2003, **425**, 667.
15 I. Loa, K. Syassen, R. Kremer, U. Schwarz and M. Hanfland, *Phys. Rev. B: Condens. Matter Mater. Phys.*, 1999, **60**, R6945.
16 A. B. Cairns, A. L. Thompson, M. G. Tucker, J. Haines and A. L. Goodwin, *J. Am. Chem. Soc.*, 2012, **134**, 4454–4456.
17 P. Serra-Crespo, A. Dikhtiarenko, E. Stavitski, J. Juan-Alcañiz, F. Kapteijn, F.-X. Coudert and J. Gascon, *CrystEngComm*, 2015, **17**, 276–280.
18 Q. Zeng, K. Wang and B. Zou, *J. Am. Chem. Soc.*, 2017, **139**, 15648–15651.
19 Y. Liu, B. Fu, W. He, W. Qiu, X. Ren, P. Zhao and W. Cai, *Cryst. Growth Des.*, 2025, **25**, 1423–1431.
20 A. B. Cairns, J. Catafesta, C. Levelut, J. Rouquette, A. Van Der Lee, L. Peters, A. L. Thompson, V. Dmitriev, J. Haines and A. L. Goodwin, *Nat. Mater.*, 2013, **12**, 212–216.
21 W. Li, M. R. Probert, M. Kosa, T. D. Bennett, A. Thirumurugan, R. P. Burwood, M. Parinello, J. A. Howard and A. K. Cheetham, *J. Am. Chem. Soc.*, 2012, **134**, 11940–11943.
22 G. Feng, W.-X. Zhang, L. Dong, W. Li, W. Cai, W. Wei, L. Ji, Z. Lin and P. Lu, *Chem. Sci.*, 2019, **10**, 1309–1315.
23 Y. Liu, B. Fu, M. Wu, W. He, D. Liu, F. Liu, L. Wang, H. Liu, K. Wang and W. Cai, *Phys. Chem. Chem. Phys.*, 2024, **26**, 1722–1728.
24 D. Jiang, T. Wen, Y. Guo, J. Liang, Z. Jiang, C. Li, K. Liu, W. Yang and Y. Wang, *Chem. Mater.*, 2022, **34**, 2764–2770.
25 S. A. Hodgson, S. J. Hunt, T. J. Sørensen, A. L. Thompson, E. M. Reynolds, S. Faulkner and A. L. Goodwin, *Eur. J. Inorg. Chem.*, 2016, **2016**, 4378–4381.
26 S. A. Hodgson, J. Adamson, S. J. Hunt, M. J. Cliffe, A. B. Cairns, A. L. Thompson, M. G. Tucker, N. P. Funnell and A. L. Goodwin, *Chem. Commun.*, 2014, **50**, 5264–5266.
27 A. L. Goodwin, D. A. Keen and M. G. Tucker, *Proc. Natl. Acad. Sci. U. S. A.*, 2008, **105**, 18708–18713.
28 M. Chen, H. L. B. Boström, D. Daisenberger, N. P. Funnell, C. J. Ridley, M. Mezouar, C. Weidenthaler and A. B. Cairns, *J. Am. Chem. Soc.*, 2025, **147**, 17946–17953.
29 S. R. Batten and K. S. Murray, *Coord. Chem. Rev.*, 2003, **246**, 103–130.
30 A. A. Yakovenko, K. W. Chapman and G. J. Halder, *Acta Crystallogr., Sect. B: Struct. Sci., Cryst. Eng. Mater.*, 2015, **71**, 252–257.
31 M. Chen, H. L. B. Boström, D. Daisenberger, N. P. Funnell, C. J. Ridley and A. B. Cairns, *Chem. Sci.*, 2026, **17**, 3700–3707.
32 C. R. Kmety, Q. Huang, J. W. Lynn, R. W. Erwin, J. L. Manson, S. McCall, J. Crow, K. L. Stevenson, J. S. Miller and A. J. Epstein, *Phys. Rev. B: Condens. Matter Mater. Phys.*, 2000, **62**, 5576.
33 M. Kurmoo and C. J. Kepert, *New J. Chem.*, 1998, **22**, 1515–1524.
34 H. Mao, J.-A. Xu and P. Bell, *J. Geophys. Res. Solid Earth*, 1986, **91**, 4673–4676.
35 M. Basham, J. Filik, M. T. Wharmby, P. C. Chang, B. El Kassaby, M. Gerring, J. Aishima, K. Levik, B. C. Pulford, I. Sikharulidze, *et al.*, *J. Synchrotron Radiat.*, 2015, **22**, 853–858.
36 J. Filik, A. Ashton, P. Chang, P. Chater, S. Day, M. Drakopoulos, M. Gerring, M. Hart, O. Magdysyuk, S. Michalik, *et al.*, *J. Appl. Crystallogr.*, 2017, **50**, 959–966.
37 H. Rietveld, *Acta Crystallogr.*, 1967, **22**, 151–152.
38 A. A. Coelho, *J. Appl. Crystallogr.*, 2018, **51**, 210–218.
39 S. Batten, P. Jensen, C. Kepert, M. Kurmoo, B. Moubaraki, K. Murray and D. Price, *J. Chem. Soc., Dalton Trans.*, 1999, 2987–2997.
40 J. L. Manson, C. R. Kmety, A. J. Epstein and J. S. Miller, *Inorg. Chem.*, 1999, **38**, 2552–2553.
41 G. Pawley, *J. Appl. Crystallogr.*, 1981, **14**, 357–361.
42 R. J. Angel, M. Alvaro and J. Gonzalez-Platas, *Z. Kristallogr. – Cryst. Mater.*, 2014, **229**, 405–419.
43 F. Birch, *Phys. Rev.*, 1947, **71**, 809.
44 F. D. Murnaghan, *Proc. Natl. Acad. Sci. U. S. A.*, 1944, **30**, 244–247.
45 M. J. Cliffe and A. L. Goodwin, *J. Appl. Crystallogr.*, 2012, **45**, 1321–1329.
46 R. J. Angel, *Rev. Mineral. Geochem.*, 2000, **41**, 35–59.
47 R. D. Shannon, *Acta Crystallogr., Sect. A*, 1976, **32**, 751–767.
48 J. L. Manson, D. W. Lee, A. L. Rheingold and J. S. Miller, *Inorg. Chem.*, 1998, **37**, 5966–5967.
49 Y. Zhang, A. Sanson, Y. Song, L. Olivi, N. Shi, L. Wang and J. Chen, *Inorg. Chem. Front.*, 2022, **9**, 2036–2042.
50 M. Chen, PhD thesis, Imperial College, London, 2024.

